Western States Section of the Combustion Institute
Spring Meeting 2016

University of Washington, Seattle, Washington
March 21-22

Nanosecond pulse plasma assisted ignition simulations at atmospheric pressure

T. Casey, J.-Y. Chen
Department of Mechanical Engineering, University of California-Berkeley
Berkeley, California 94720, USA

Ignition assistance by a pulsed applied voltage is investigated in a canonical one-dimensional configuration. An incipient ignition kernel, formed by localized energy deposition into a lean mixture of methane and air at atmospheric pressure, is subjected to sub-breakdown electric fields by a DC potential applied across the domain, resulting in non-thermal behavior of the electron sub-fluid formed during the discharge. A two-fluid approach is employed to couple thermal neutrals and ions to the non-thermal electrons, and a two-temperature plasma mechanism describing gas phase combustion, excitation of neutral species, and high-energy electron kinetics is employed to account for non-thermal chemical effects. Charged species transported from the ignition zone drift rapidly through the domain, augmenting the magnitude of the electric field in the fresh gas during the pulse through a dynamic-electrode effect, which results in an increase in the energy of the electrons in the fresh mixture with increasing time. Enhanced fuel and oxidizer decomposition due to electron impact dissociation and interaction with excited neutrals generate a pool of radicals, mostly O and H, in the fresh gas ahead of the flame's preheat zone. The effect of the nanosecond pulse is to increase the mass of fuel burned at equivalent times relative to the unsupported ignition through enhanced radical generation, resulting in an increased heat release rate in the immediate aftermath of the pulse.

1 Introduction

Flames act as weakly ionized plasmas, generating weak self-induced electric fields due to local charge separation over small distances of length comparable to the reaction zone. As such, externally applied electric fields have the potential to augment flame behavior non-intrusively. Investigations of applied electric fields have shown the ability to enhance burning velocities [1], stabilize flames near flammability limits [2], and support ignition [3]. If the strength of the electric field is high enough to produce a sufficient level of non-thermal electrons, it is understood that enhancement occurs due to fragmentation of fresh gas molecules resulting in an increased population of reactive intermediates such as O and H [4]. In the context of ignition, simulations of multiple nanosecond pulsed plasma discharges in n-heptane have been shown to decrease ignition delay time significantly [5] through the generation of non-thermal electron plasma in a breakdown process. Furthermore, it has been demonstrated experimentally that microwave frequency electric field excitation reduces the flame development time of inductive spark ignition of methane-air mixtures in a constant volume chamber [3]. The experiments in Ref. [3] suggested that enhancement arises as a result of flame wrinkling due to the perturbative effect of the applied field, indicating that both chemistry and hydrodynamics play important roles. As a practical concern to ignition strategies based on breakdown discharges, increasing the energy of the discharge itself (e.g. increasing the spark energy) can have undesirable

effects in terms of device wear due to electrode ablation, which presents significant challenges for igniting lean high-pressure mixtures typical of future advanced engine technologies. As such, it is desirable to investigate means of ignition and ignition-support that occur in the sub-breakdown regime that deliver necessary performance, while avoiding excessive device wear. Furthermore, with increasing interest in using natural gas as a clean fuel alternative, the plasma-assisted ignition of methane is an important process due to the difficulty of initiating the first H abstraction from CH_4. Analysis of non-thermal electron transport properties and energy coupling to bulk mixtures in the sub-breakdown regime in premixed methane-air flames suggests a breakdown threshold of approximately 150Td [6]. The purpose of this paper is to investigate sub-breakdown electric field assisted combustion of an established ignition kernel at device relevant pressure, in order to shed light on the multiple electrodynamic and chemical processes involved in increasing the overall mass of fuel burned as a result of a nanosecond pulse.

2 Configuration and modeling

The physical domain is a 1cm region filled with premixed methane and air (79% N_2 and 21% O_2 by volume) with equivalence ratio 0.5 at 1atm. The boundaries are open fluid outlets with imposed potentials, conceptually representing wire mesh electrodes unobstructive to fluid. This configuration is chosen such that the ignition event occurs at constant pressure. The nanosecond pulse is applied with positive 4.5kV and negative 4.5kV on the left and right electrodes respectively, for a total of 9kV across the domain. Pulses are applied for up to a maximum of 35 ns. These pulse parameters are chosen to represent the typical values employed in constant-volume methane-air plasma ignition experiments conducted in our lab.

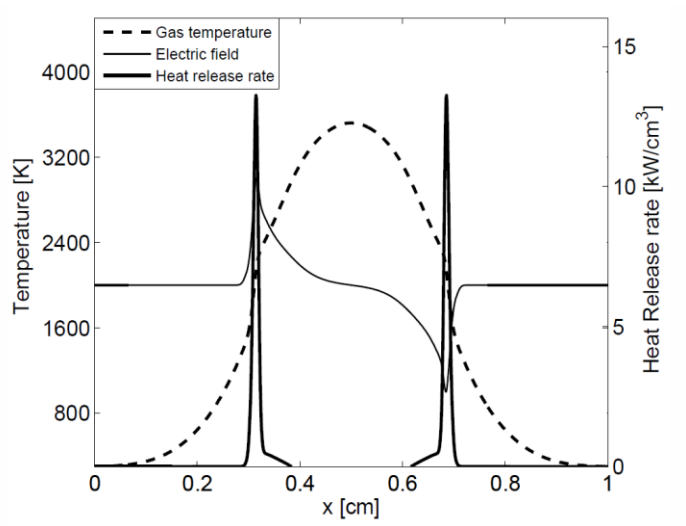

Figure 1: Instantaneous gas phase temperature, heat release rate, and electric field (arbitrary unit) just prior to the application of the external potential. A hot burned gas zone supports the rapid outward propagation of heat release rate fronts where charged species are produced. The peak electric field strength is 0.5 Vcm^{-1}. The zero gradient of the electric field in the fresh gas indicates the absence of charge density.

2.1 Models and approximations

The two-temperature methane-air plasma mechanism is built upon the GRI-Mech 3.0 methane-air mechanism [7]. Ion chemistry pathways containing thermal electrons are added following the mechanism in Ref. [8].

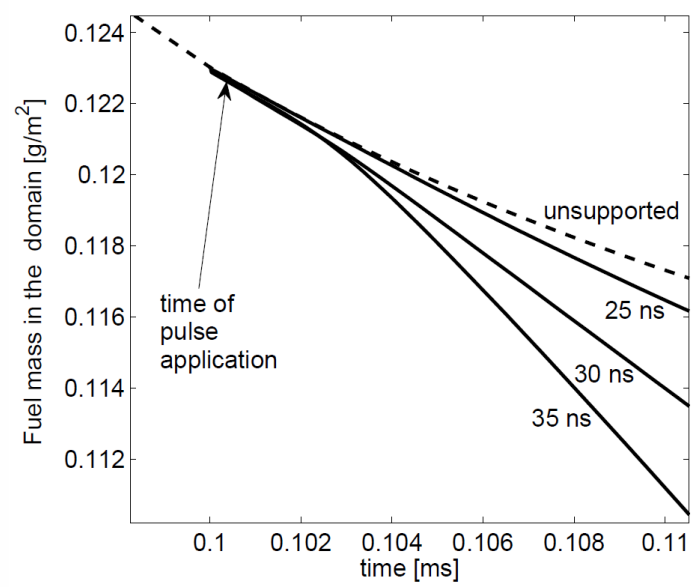

Figure 2: Ignition enhancement as a function of voltage pulse width, quantified by the remaining fuel mass in the domain as a function of time.

The rates of inelastic electron impact reactions, resulting in the decomposition of neutral molecules, ionizations, and excitations, are precomputed using a representative lean unreacted methane-air mixture and parameterized by the electron temperature using available CHEMKIN fitting [9]. Collision cross-section data for these electron neutral interactions are obtained from the LXCat database [10, 11]. Mechanism reduction is performed using ignition delay targets via the TSA algorithm [12] for lean methane-air mixtures at 300K, 1atm, using a variety of initial electron densities and electric fields.

2.2 Numerics

A compressible reacting flow solver employing high-order central differencing and an explicit Runge-Kutta time integration scheme is used to advance the conservation equations governing the planar ignition problem. The outlet boundaries are implemented in the governing equations using a non-reflecting treatment based on characteristics [13].The Poisson equation for Gauss's Law for the electric potential is solved using a geometric multi-grid scheme. Electron fluxes are specified in the drift-diffusion limit (i.e. zero electron inertia approximation [14]) using transport coefficients calculated using the BOLSIG+ solver [15]. The electron temperature is obtained from BOLSIG+ given the neutral mixture and local reduced electric field. Ion-mobilities are set equal to $1\text{cm}^2\ \text{V}^{-1}\text{s}^{-1}$ [16, 17]. For computational efficiency, BOLSIG+ electron data are calculated a-priori and retrieved with efficient queries from databases at runtime. Mixture dependency is included by constructing a multi-dimensional interpolation space consisting of the major neutral species. The transport data for electronically excited species is assumed to be the same as the ground state equivalents. Due to the explicit time integration scheme, the time scales of the plasma chemistry must be resolved for numerical stability. As such, the time step employed during the high voltage pulse is $\Delta t = O(10^{-13}\text{s})$. Post pulse, the time step relaxes back to the time scales associated with the gas phase chemistry, typically $\Delta t = O(10^{-9}\text{s})$. A uniform mesh of 1280 grid points is used ($\Delta x \approx 7.8\mu\text{m}$) with the computational domain decomposed spatially in parallel using the MPI (message passing interface) framework.

3 Results and Discussion

3.1 Overview of ignition enhancement

At the start of the simulation, ignition is initiated using a Gaussian energy source. Figure 1 shows the gas temperature, heat release rate, and electric field profile 0.1ms into the simulation. The 9kV DC voltage is applied as a step function after 0.1ms has elapsed, with the voltage sustained for as little as 25ns or as long as 35ns. A pool of charged species exists in the reaction zones due to chemi-ionization prior to the application of the electrical pulse, which subsequently generate further electrons through ionization processes. The overall effect of the pulse duration is measured in terms of the temporal evolution of the remaining fuel mass as shown in Fig. 2. It is seen that the remaining fuel mass is essentially unchanged during the pulse but begins to deviate from the unsupported solution after approximately 20μs. No enhancement is observed for pulse lengths shorter than 20ns, indicating that a threshold of plasma chemistry activation is achieved for longer pulses with a sustained high electron temperature.

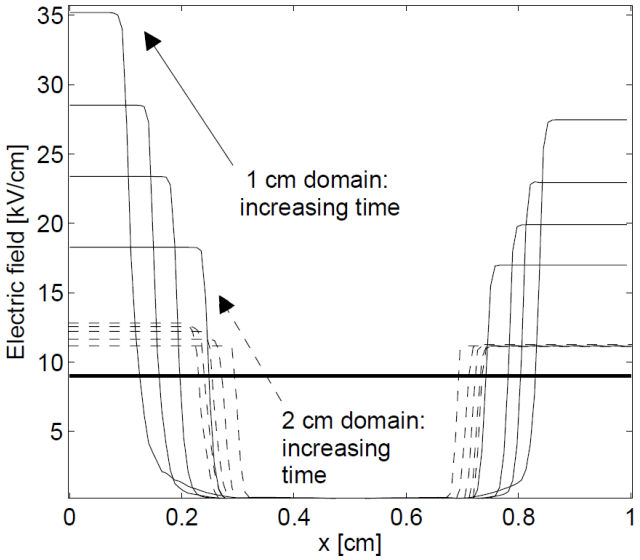

Figure 3: Effect of domain size on the electric field strength ahead of the charge fronts in the fresh gases at four time instants during the pulse: 5, 10, 15, and 20ns. The horizontal line represents the electric field in a domain with zero charge, which is the same for both configurations.

3.2 Electrodynamics of charge fronts

As a 9kV voltage is applied across the domain, an electric field pointing towards the right of the domain is established. Under the influence of the electric field, charged species are transported from the flame zone into the fresh gases where electrons take part in further ionization processes, with the electrons and anions transported to the left and the cations to the right. At the same time, the burned gas loses most of its net charge, although the density of charged species remains high and is characterized by an electric field close to zero along with zero potential. The electric field is shown in Fig. 3 (1cm case), with zero electric field in the burned gas for all times.

The concentration of charge in the outwardly propagating fronts (Fig. 4) results in a floating electrode effect, such that changes in the electric field are restricted to regions in the immediate vicinity of the fronts. Across the charge fronts, the potential increases abruptly from zero in the burned gases to a linear distribution in the fresh gas, where there is close to zero charge density and the electric field strength is constant (Fig. 3). Figure 4 provides a close look at the dynamics of the electrons prior, during, and after the nanoscale voltage pulse.

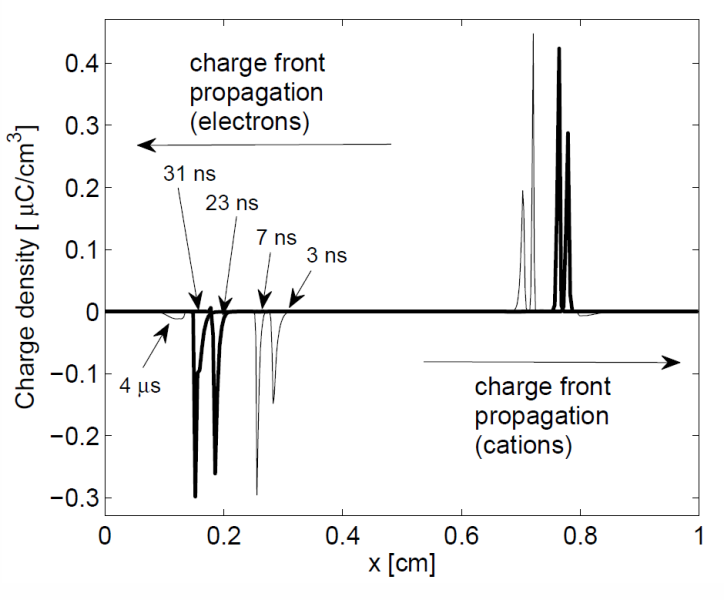

Figure 4: Outward propagation of charge fronts, electrons (left) and cations (right), originating from the flame zone and burned gas and enhanced by ionization.

From 3 ns to 7ns the electron density in the fresh gas on the left side of the domain builds up as electrons, now non-thermal, take part in impact ionization processes as they transit toward the left boundary electrode. At the same time, the positive charge front made up of cations on the right side of the domain builds up due to ionization of fresh gas molecules by non-thermal electrons, initially present at low concentration in the fresh gas due to diffusion from the flame zone prior to the pulse, as they drift to the left. These electrons will tend to remain near the positive right propagating charge front due to the large change in electric field that occurs in its vicinity, hindering their leftward drift motion. Towards the end of the pulse from 23ns to 31ns, the charge front continue to propagate outwards, with the left moving negative charge front, comprised primarily of electrons, advancing further than its cation analog. Post pulse, the charge fronts collapses due to recombination, as shown by the profile at 4 μs. As the fronts advance toward the electrodes at the boundaries, the electric field strength in the fresh gas increases driving a further increase in electron temperature in the fresh gases. This compression of the electric potential in the fresh gas introduces a length scale in the problem, since the degree of compression depends on the separation between the fronts and the boundaries where the electrodes are located. Figure 3 compares the electric field strength for the 1 cm domain with 9kV applied voltage to the case of a 2cm domain with 18kV voltage difference (i.e. equivalent initial effective electric field strength). It is apparent that increasing the separation between the electrode and the charge front decreases the magnitude of the electric field strength in the fresh gas relative to the smaller domain with 9kV.

3.3 Nanosecond pulse chemistry

Prior to the application of the 9kV DC pulse, the decomposition of CH_4 in the regions of the domain ahead of the propagating reactive fronts is dominated by H abstraction reactions by the radicals, OH, H, and O, with the dominant heat release pathways being oxidation of CH_3 by atomic O through:

$$O + CH_3 \longleftrightarrow H + CH_2O \qquad (1)$$

and

$$O + CH_3 \longleftrightarrow H + H_2 + CO. \qquad (2)$$

Oxidizer decomposition is dominated by the chain branching reaction:

$$H + O_2 \longleftrightarrow O + OH. \qquad (3)$$

For the case of unsupported ignition, these pathways persist as the primary means of decomposition and heat release up to later times. Immediately after the DC pulse is turned on, and a sufficient population of non-thermal electrons is generated, the decomposition of CH_4 occurs almost entirely by electron impact dissociation, which is represented in Fig. 5 at the time instant labeled "1" by the reaction:

$$e^- + CH_4 \rightarrow e^- + CH + H_2 + H \qquad (4)$$

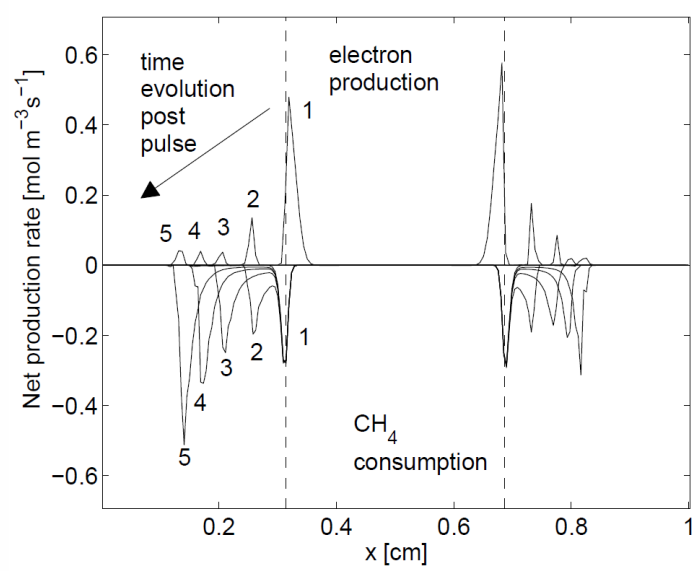

Figure 5: Production rate of electrons (top half plane) and consumption of CH_4 (bottom half plane) during the pulse at five time instants corresponding to 1, 4, 8, 12, and 16ns labeled "1" to "5".

The dashed lines indicate the location of the reaction front (peak heat release rate), which does not vary during the nanoscale pulse while oxidizer decomposition occurs through impact ionization:

$$e^- + O_2 \rightarrow 2e^- + O_2^+ \qquad (5)$$

and dissociation:

$$e^- + O_2 \rightarrow e^- + 2O. \qquad (6)$$

This ionization reaction is almost entirely responsible for producing electrons at this stage of the pulse. Electron production is at a maximum at this early stage of the pulse, as shown by the time 1 electron production profile in Fig. 5. This can be attributed to the thermal electron pool concentrated in the flame zone prior to the pulse, which subsequently takes part in ionization reactions with abundant O_2 and N_2 in the flame zone, although primarily with O_2 due to its lower ionization energy, i.e. 12.06 eV for O_2 compared to 15.58 eV for N_2. After 5ns from the onset of the pulse, the charge fronts have propagated appreciably into the fresh gas and are essentially separated from the flame zones. Increasing electron energy in the fresh gases accelerates the impact excitation of abundant N_2.

Analysis of the chemical pathways for the decomposition of fuel and oxidizer in the flame zones, where the electric field is now close to zero and the electron temperature is low, shows that the dominant reactions are those that were identified prior to the pulse, i.e. abstraction reactions by radicals. At this stage, fuel decomposition by electron impact reactions takes place further into the fresh gas in the vicinity of the advancing charge fronts (time 2), and the rate of CH_4 consumption in these regions is comparable to that taking place in the flame zone by radical abstraction. The consumption of fuel and oxidizer in these regions near the charge fronts arises from both electron impact dissociation as well as de-excitation reactions of electronically excited N_2 molecules, N_2(B3), N_2(C3), and N_2(a′), in contrast to electron impact processes that dominated in the immediate aftermath of the pulse application.

The charge density in the outwardly propagating fronts is enhanced by impact ionizations of the fresh gas neutrals, mostly the abundant N_2, which is now favored over O_2 as the electron energy is now high enough to overcome the higher ionization energy of N_2. For times 3, 4, and 5, the rate of electron production is relatively unchanged, indicating that ionization processes have not accelerated markedly despite the increase in electron energy due to the increasing electric field, but impact dissociation, and excitation and de-excitation processes do increase the magnitude of the CH_4 consumption rate from time 3 to time 5 by about a factor of 2.

3.4 Radical profiles

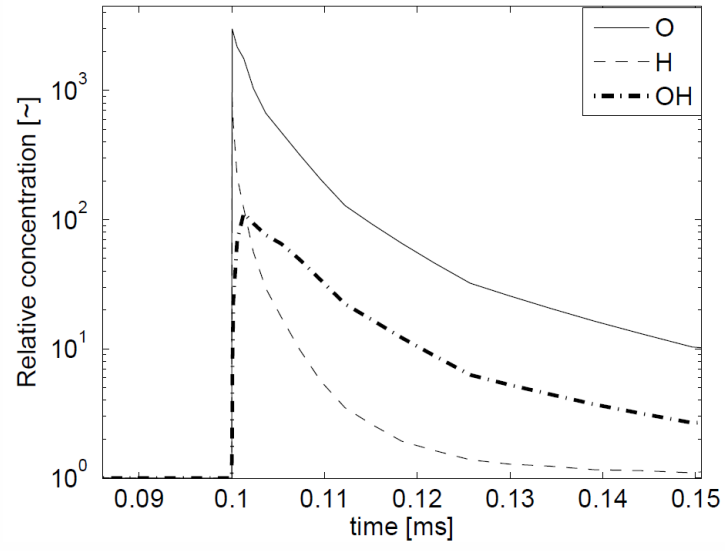

Figure 6: Evolution of spatially-averaged major radical species concentrations for a 35ns pulse normalized by the evolution in the unsupported case.

To analyze the enhancement of radical formation in the fresh gas due to the action of the applied voltage, the radical concentrations are integrated spatially between the electrodes and a fixed location, chosen to be the locations of the reaction fronts prior to the application of the voltage pulse. Prior to the pulse, the fresh gas concentrations are ssentially zero, during the pulse the concentrations of O and H build up due to non-thermal electron processes, while after the pulse these concentrations decrease due to recombination. The decrease is compensated in part by the positive contribution of diffusion from the burned gases as the flame fronts advance. Figure 6 shows the rapid build-up of major radicals during the application of the 35ns pulse, with radical concentrations slowly relaxing to the values of the unsupported case post-pulse.

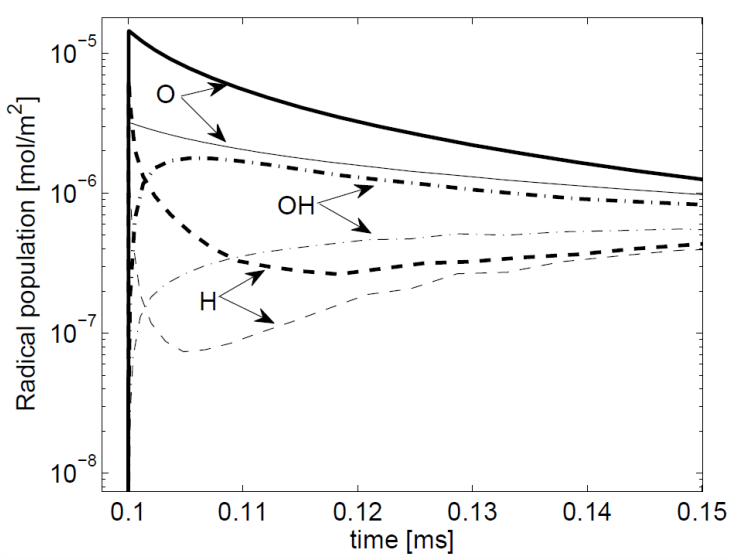

Figure 7: Evolution of total populations of major radical species for a 35ns (solid lines) and 26 ns (dashed lines) pulse.

Once the pulse is deactivated, recombination depletes the populations of O and H rapidly, resulting in the production of OH. The O population decreases at a much slower rate post pulse than H. Comparing the 35ns case to a shorter duration pulse (Fig. 7) highlights the degree to which the radical build up is sensitive to the pulse length. Shortening the pulse by approximately 25% results in a factor of 4-5decrease in the total domain integrated radical populations.

Figure 8 shows the analysis of the spatial distribution of the radicals during and post pulse in the left side fresh gas, indicating that the OH concentration is unaffected in the fresh gas and close to the flame zone during the pulse when the recombination chemistry is essentially frozen, but grows post pulse as the pool of O and H radicals recombine. Figure 8 also shows that the contribution to overall O and H generation is mostly towards the end of the pulse, with the spatial profiles of both reaching their maxima in the regions close to the boundaries where the fresh gas electric field strength is at its highest. The populations slowly build up (solid lines) before reaching maxima in the vicinity of the boundary. The spatial character of the profiles is such that O and H deep in the fresh gas have the propensity to migrate back towards the flame zone through diffusion even as recombination is taking place. Peaks in the post pulse OH profiles occur in the vicinity of the O and H maxima but also close to the flame zone, suggesting that the balance of the radicals in this region is affected by diffusion of O and H before these are consumed in the flame zone. The consequence of the pulse for CH_4 consumption is to advance the outward propagation of the CH_4 profile relative to the unsupported case. The heat release rate is similarly augmented, with the heat release rate fronts in the supported case leading those in the unsupported one as they advance into the fresh gas.

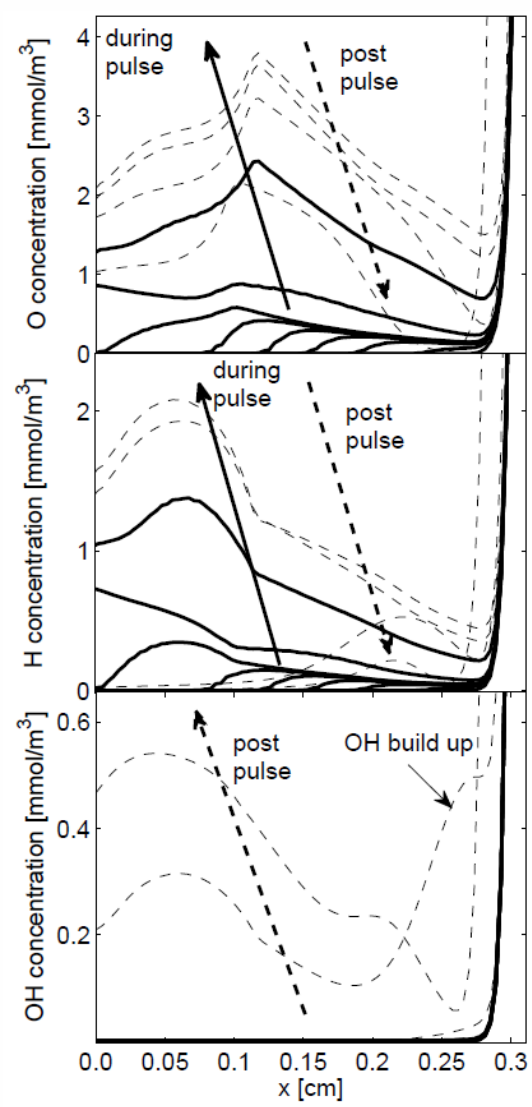

Figure 8: Evolution of radical species spatial profiles during the pulse (solid lines) and post pulse (dashed lines). The profiles are separated in time by 4 ns during the pulse, with the post pulse profiles taken at 1ns, 56ns, 1.7µs, and 2µs after the pulse has ended. The OH pool in front of the flame post pulse is entirely due to O and H recombination.

As the heat release rate fronts advance, their magnitudes diminish (time instants 1, 2, 3) due to the diminished heat flux support supplied by the burned gases as the flames propagate outwards. The total domain integrated heat release rate for the 35ns and unsupported cases are shown in Fig. 10. This metric provides a measure of the enhancement of the overall reactivity. In the immediate aftermath of the pulse when the radical populations are at a maximum, the heat release rate experiences a spike, followed by a rapid and then gentle decay as radicals recombine to form OH. Once the OH population has reached a maximum post pulse (at approximately 0.105ms as indicated in Fig. 7 for the 35ns case), the heat release rate begins to decay much slower, supported by an enhanced OH pool.

In addition to the chemical interactions driven by high-energy electrons, thermal energy transfer between the electrons and the neutrals and ions occur due to elastic and inelastic collisional processes, increasing the temperature of the bulk gas. The influence of these interactions was investigated by omitting these coupling terms from the right-hand-side of the bulk gas energy equation. The effect on fuel mass consumption was almost negligible, indicating that the major enhancement effect is chemical in nature.

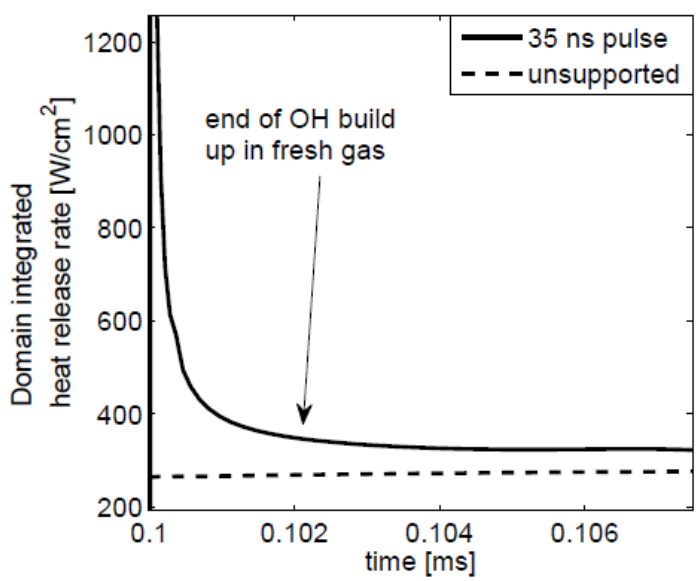

Figure 10: Comparison of the evolution of the domain integrated heat release rate in the post-pulse period for a 35ns pulse (solid line) and the unsupported case (dashed line).

While DC pulses are characterized by enhanced fresh gas electric field magnitude, the transport of electrons from the reaction zones may result in diminished electron concentration in the immediate vicinity of these zones and mitigate the rates of electron impact reactions. AC pulses of sufficiently high frequency have the capability to confine electrons close to where they are created due to the resulting alternating electron drift flux. Figure 11 shows the results of AC pulses of frequency 2.45GHz compared to DC pulses. It is apparent that the consumption of fuel is initially accentuated for pulses of equivalent duration, which can be attributed to more vigorous radical production in the immediate vicinity of the reactions zones due to enhanced impact decomposition.

4 Conclusions

The effect of a nanosecond applied voltage on a developing ignition kernel at 1atm pressure was studied numerically using a two-fluid solver with two-temperature chemistry to represent non-thermal electron processes. Fuel and oxidizer decomposition in the fresh gases is enhanced by the propagation of charge fronts introducing a dynamic electrode effect, which acts to increase the fresh gas electric field, and thus the electron energy, accelerating electron impact processes. Fuel and oxidizer fragments in the fresh gas recombine to form an enhanced pool of OH in front of the outwardly propagating flame fronts, causing an enhancement of fuel consumption. The relatively modest ignition enhancement by a single pulse suggests that a strategy consisting of multiple pulses in sequence may sustain an enhanced radical pool, opening up a large design space for determining optimal and novel pulsing strategies for practical regimes of interest. AC fields appear to be a promising option for further enhancement. In closing, we note that multi-dimensional simulations ultimately are required to investigate the possibility of inducing flame wrinkling or hydrodynamic instability through heat-release perturbations induced by pulsed voltages.

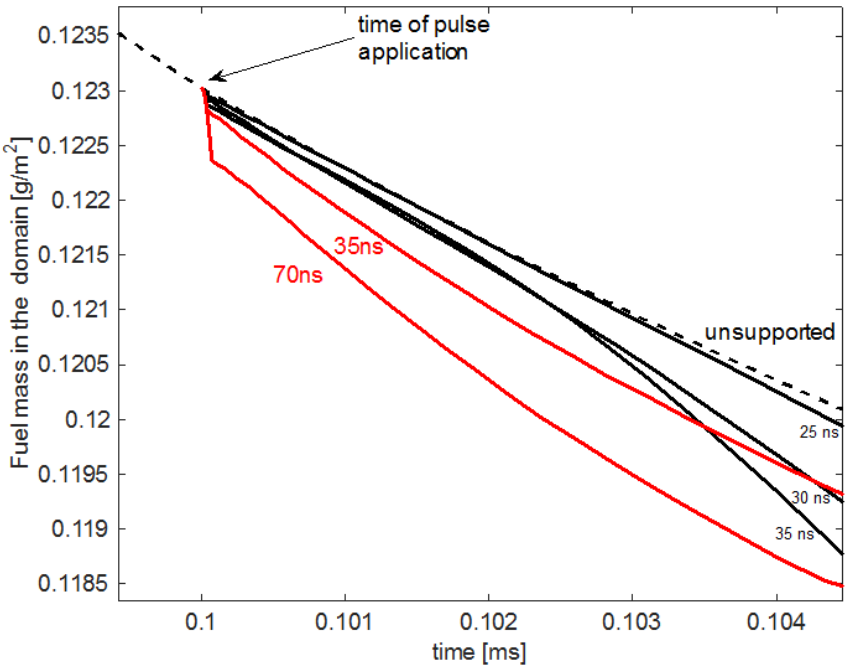

Figure 11: Comparison of AC pulses (red) and DC pulses (black, solid) with respect to the remaining fuel mass in the domain as a function of time.

References

[1] H. Jaggers, A. Von Engel, The effect of electric fields on the burning velocity of various flames, Combust. Flame 16 (1971) 275–285.
[2] M. S. Bak, H. Do, M. G. Mungal, M. A. Cappelli, Plasma-assisted stabilization of laminar premixed methane/air flames around the lean flammability limit, Combust. Flame 159 (2012) 3128–3137.
[3] B. Wolk, A. DeFilippo, J.-Y. Chen, R. Dibble, A. Nishiyama, Y. Ikeda, Enhancement of flame development by microwave-assisted spark ignition in constant volume combustion chamber, Combust. Flame 160 (2013) 1225–1234.
[4] Y. Ju, W. Sun, Plasma assisted combustion: Dynamics and chemistry, Prog. Energ. Combust. Sci. 48 (2015) 21–83.
[5] S. Nagaraja, W. Sun, V. Yang, Effect of non-equilibrium plasma on two-stage ignition of n-heptane, Proc. Combust. Inst. 35 (2015) 3497–3504.
[6] F. Bisetti, M. E. Morsli, Kinetic parameters, collision rates, energy exchanges and transport coefficients of non-thermal electrons in premixed flames at sub-breakdown electric field strengths, Combust. Theor. Model. (2014).
[7] G. P. Smith, D. M. Golden, M. Frenklach, N. W. Moriarty, B. Eiteneer, M. Goldenberg, C. T. Bowman, R. K. Hanson, S. Song, W. C. Gardiner Jr, et al., GRI-mech 3.0, available at <http://www.me.berkeley.edu/gri_mech/>, (1999).
[8] J. Prager, U. Riedel, J. Warnatz, Modeling ion chemistry and charged species diffusion in lean methane–oxygen flames, Proc. Combust. Inst. 31 (2007) 1129–1137.

[9] R. K. Janev, W. D. Langer, D. E. Post Jr, K. Evans Jr, Elementary processes in hydrogen-helium plasmas: cross sections and reaction rate coefficients, volume 4, 1987.
[10] S. Pancheshnyi, S. Biagi, M. Bordage, G. Hagelaar, W. Morgan, A. Phelps, L. Pitchford, The LXCat project: Electron scattering cross sections and swarm parameters for low temperature plasma modeling, Chem. Phys. 398 (2012) 148–153.
[11] A. C. DeFilippo, Microwave-Assisted Ignition for Improved Internal Combustion Engine Efficiency, PhD Thesis, University of California, Berkeley, 2013.
[12] Y. Tham, F. Bisetti, J.-Y. Chen, Development of a highly reduced mechanism for iso-octane HCCI combustion with targeted search algorithm, J. Eng. Gas Turb. Power 130 (2008) 042804.
[13] C. S. Yoo, H. G. Im, Characteristic boundary conditions for simulations of compressible reacting flows with multi-dimensional, viscous and reaction effects, Combust. Theor. Model. 11 (2007) 259–286.
[14] T. Nitschke, D. Graves, A comparison of particle in cell and fluid model simulations of low-pressure radio frequency discharges, J. Appl. Phys. 76 (1994) 5646–5660.
[15] G. Hagelaar, L. Pitchford, Solving the Boltzmann equation to obtain electron transport coefficients and rate coefficients for fluid models, Plasma Sources Sci. Tech. 14 (2005) 722.
[16] A. Fialkov, Investigations on ions in flames, Prog. Energy Combust. Sci. 23 (1997) 399–528.
[17] M. Belhi, P. Domingo, P. Vervisch, Modelling of the effect of DC and AC electric fields on the stability of a lifted diffusion methane/air flame, Combust. Theor. Model. (2013).